Biosensors and Bioelectronics 190 (2021) 113423

Contents lists available at ScienceDirect

Biosensors and Bioelectronics

journal homepage: www.elsevier.com/locate/bios

# Highly sensitive wide-range target fluorescence biosensors of high-emittance metasurfaces

Masanobu Iwanaga

*Research Center for Functional Materials, National Institute for Materials Science (NIMS), 1-1 Namiki, Tsukuba, 305-0044, Japan*

ARTICLE INFO

*Keywords:*
Fluorescence sensing
Metasurface biosensor
Microfluidic path
IgG
anti-p53 antibody
Nucleic acid
SARS-CoV-2
DNA
Micro-RNA

ABSTRACT

We demonstrate highly sensitive fluorescence (FL) biosensors made of plasmon–photon-hybrid high-emittance metasurfaces, which are hybrid structures composed of perforated silicon waveguides and stacked complementary (SC) gold nanostructures. The SC metasurfaces are applicable to a wide range of targets from antibodies to nucleic acids. As a test bed, a representative antibody of immunoglobulin G is immobilized on the metasurfaces through microfluidic paths and then is directly detected in a scaled manner even at a very low concentration of 5 pg $mL^{-1}$, *i.e.*, 34 fM. Moreover, a cancer marker of p53 antibody is indirectly detected on the SC metasurfaces at a low concentration of 50 pg $mL^{-1}$, which is significantly lower than the medical diagnosis criterion of a few ng $mL^{-1}$. Furthermore, single-strand DNAs that are oligonucleotides and complementary to SARS-CoV-2 RNA are detected with 1 h immobilization time in the range of fmol $mL^{-1}$ in a scaled manner. These experimental results indicate that the present FL metasurface sensors function efficiently as biosensors for a wide range of biomarkers.

## 1. Introduction

Commercial standard optical biosensing methods, such as enzyme-linked immunosorbent assay (ELISA), have been performed on plastic microplates. These plates themselves cannot enhance optical signals from objects; the primary role is to immobilize biomolecules with a small volume of reagents on the order of 0.1 mL. ELISA is usually used to evaluate protein molecules, enabling the limit of detection (LOD) at approximately 1 pM in transmission measurements at 450 nm (Giljohann and Mirkin (2009)).

It is an intriguing issue to attain prominently enhanced optical signals on platforms other than the plastic plates. Surface-enhanced Raman scattering (Nie and Emory (1997); Kneipp et al. (1997)) and plasmon-enhanced fluorescence (FL) (Lakowicz et al. (2008); Bauch et al. (2014)) were stimulated by this motive. Raman scattering is suitable for analyzing small molecules because molecular vibration modes have to be assigned. For macromolecules such as protein molecules with a molecular weight more than 50000, it is generally difficult to resolve the vibration modes; consequently, Raman scattering becomes an ineffective method for detecting the giant biomolecules. Instead, FL detection has been widely used for the biomolecules, since FL labeling ensures the specific detection of target molecules in biosensing.

To date, numerous studies have been performed investigate on FL-enhancing effects in plasmonic platforms. Among them, some prominent results have been reported, including FL-intensity enhancement exceeding 1000-fold in comparison with relevant reference substrates (Kinkhabwala et al. (2009); Schmelzeisen et al. (2010); Fu et al. (2010); Zhang et al. (2012); Zhou et al. (2012); Punj et al. (2013); Choi et al. (2015); Iwanaga et al. (2016)). Although such studies pertained to biosensing, studies that demonstrate the practical capability of FL-enhancing plasmonic platforms as biosensors for detecting practical disease markers are few.

In this article, we demonstrate that the plasmon–photon-hybrid metasurfaces (Iwanaga and Choi (2015); Choi et al. (2015); Iwanaga et al. (2016)) serve as practical biosensors for a wide range of targets from antibodies (Abs) to DNAs. The structure of a plasmon–photon-hybrid metasurface is illustrated in Fig. 1A; it comprises a silicon slab waveguide with a nanohole array and stacked complementary (SC) gold nanostructures. We refer to the plasmon–photon-hybrid metasurfaces as SC metasurfaces, based on the structural features. The prominent FL-intensity enhancement exceeding 2000 folds for flat silicon wafers was experimentally demonstrated (Choi et al. (2015); Iwanaga et al. (2016)). This prominent enhancement is enabled by the total management of light absorption, suppression of FL-quenching energy transfer, and high emittance at FL wavelengths (Iwanaga (2016)). Consequently, the SC metasurfaces do not rely only on local

*E-mail address:* iwanaga.masanobu@nims.go.jp.

https://doi.org/10.1016/j.bios.2021.113423
Received 1 April 2021; Received in revised form 25 May 2021; Accepted 6 June 2021
Available online 11 June 2021

electric-field enhancement, and the FL-enhancement effects are quite uniform and reproducible. Although it is widely believed that intense local electric fields (or hot spots) are a primary key factor to obtain prominent FL enhancement, the hot spots always result in inhomogeneous enhancing responses and adversely affect the reproducibility of the enhanced signals.

The SC metasurfaces were considered a good platform for FL biosensing; however, this has not been validated. In this study, for the proof of concept, a representative Ab of immunoglobulin G (IgG), a cancer marker anti-p53 Ab, and a DNA complementary to RNA of SARS-CoV-2 were selected as targets. They were detected on the SC metasurfaces through enhanced FL signals.

## 2. Experimental section

### 2.1. Metasurface sensor chips

The nanostructure (top) of the SC metasurfaces in this study and a wide view (bottom) are illustrated in Fig. 1A. The SC metasurfaces have a series of resonances associated with large light absorption bands (Iwanaga and Choi (2015)). Owing to reciprocity (Greffet and Nieto-Vesperinas (1998)), the large absorption is equivalent to high emittance from the metasurfaces. We adjusted the high-emittance band to FL wavelengths of interest in this study as it was reported that the structural parameters can change the resonant high-emittance band (Iwanaga et al. (2015)).

The metasurface substrates were fabricated using electron beam lithography (EBL). Silicon-on-insulator (SOI) wafers of 6 inch diameter were diced into 2 cm squares prior to the EBL process. The SOI wafers comprised stacked layers on a base silicon wafer of 675 $\mu$m thickness: the top SOI layer of 200 nm thickness and the second layer of buried oxide (*i.e.*, $SiO_2$) of 375 nm thickness. The EBL process started with high-precision nanopatterning on a spin-coated resist film using an electron-beam drawing instrument (JBX-6300FS, JEOL, Tokyo, Japan), and then the SOI layer was dry etched selectively. Finally, the residual resist in the EBL process was removed in oxygen plasma. The SOI nanostructures were designed to be a periodic hexagonal array of air holes; the periodic length was set to 410 nm and the diameters of the air holes were set to 260 or 300 nm. By depositing an underlying titanium layer of 0.8 nm thickness and a gold film of 30 nm thickness normally onto the SOI nanostructured substrates, we prepared the metasurfaces of SC structures as illustrated in Fig. 1A and experimentally confirmed the SC structures as shown in Fig. 1B. A top-view scanning-electron-microscopy (SEM) image is shown in Fig. 1C; the air-hole diameter is approximately 300 nm, as designed. The thin titanium layer was introduced to ensure that the gold layers adhered to the SOI and $SiO_2$ outermost surfaces; the titanium layer was so thin that it hardly affected optical resonances in the SC metasurfaces.

The dimensions of the metasurface were designed to fit microfluidic (MF) paths, being typically $0.72 \times 0.72$ or $1.2 \times 0.72$ mm$^2$. The MF chips were made of polydimethylsiloxane (PDMS) and were transparent in the visible wavelengths. Fig. 1D shows a photograph of the metasurface sensor chip, which is a self-absorbed pair comprising a metasurface substrate and a PDMS MF chip. The photograph was taken when the holder cover was removed; the cover held MF tubes (Tygon ND-100-80, Cole-Parmer, IL, USA) that enabled liquid reagents to flow into the metasurface chip and out from the chip. The directions of the liquid reagents including proteins and DNAs are schematically indicated with curved arrows. For proof-of-concept experiments, we prepared the MF system with three channels; however, in principle, the number of channels can be increased.

### 2.2. MF system

A schematic diagram of the MF system, which includes the metasurface sensor, is shown in Fig. 1E. A pressure controller (OB1, ELVEFLOW, Paris, France) was supplied with $N_2$ gas, and it precisely controlled the pressure to each microtube. The flow rate in the metasurface sensor chip ranged from 4 to 12 $\mu$L min$^{-1}$. When only buffers flowed into the metasurface chips, we set the flow rate to approximately 10 $\mu$L min$^{-1}$. When the reagents including proteins and DNAs flowed into the metasurface chip, we set the flow rate to approximately 5 $\mu$L min$^{-1}$.

A section transverse to the MF path is schematically illustrated in Fig. 1F, where the liquid flows in a direction transverse to the sheet (or the screen). The height of the MF path was 30 $\mu$m, whereas the height of SC metasurface was 230 nm. Hence, the MF path was significantly higher than the metasurface layer.

### 2.3. Preparations for metasurfaces and biosamples

A carboxy-acid (CA) self-assembled monolayer (SAM) was

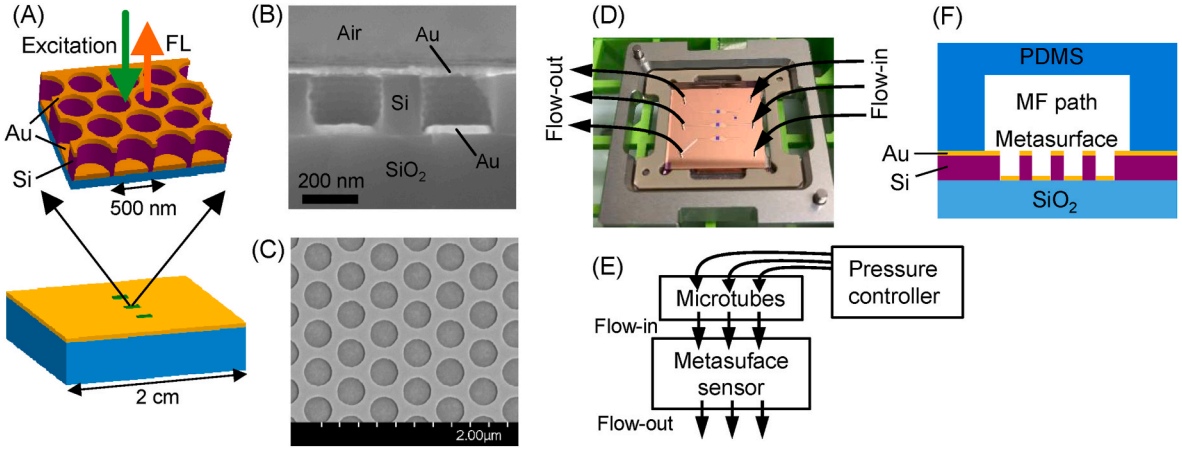


**Fig. 1.** (A) Plasmon–photon-hybrid metasurface composed of stacked complementary (SC) structures regarding gold nanostructures. Wide-view and magnified illustrations are shown at bottom and top, respectively. Directions of light excitation and fluorescence (FL) emission are indicated by arrows. (B) Section-view scanning-electron-microscopy (SEM) image exhibiting typical SC structure. Scale bar indicates 200 nm. (C) Top-view SEM image of SC structure composed of circular hole array. Periodic length and diameter are approximately 410 and 300 nm, respectively. (D) Photograph of metasurface sensor chip. Liquid flowing in/out of the microfluidic (MF) channels are schematically depicted. (E) Diagram of MF system including the metasurface sensor. (F) Section-view illustration of metasurface sensor chip, consisting of SC metasurface substrate and polydimethylsiloxane (PDMS) chip. Section was set to be transverse to MF path. (For interpretation of the references to color in this figure legend, the reader is referred to the Web version of this article.)

introduced on outermost gold surface in the SC structure using a commercial kit (C488, Dojindo Molecular Technologies, MD, USA). It was reported that a CA SAM enables the oriented immobilization of Abs, owing to the coexistence of carboxy- and hydroxy-ends (Kyo et al. (2005)). The SC metasurface substrates were washed in ethanol by applying ultrasonic waves for 5 min and immersed overnight in CA-SAM ethanol solution of 100 $\mu$M. The CA-SAM-grown metasurface substrates were rinsed in ethanol and successively washed in purified water under ultrasonic-wave application; each step was performed for 5 min. Finally, the CA-SAM-grown metasurface substrates were dried with blowing $N_2$ gas and then stored at 5°C in a $N_2$ atmosphere until they were used in experiment.

When the CA-SAM metasurface substrates were used, the SAM was activated using an amine-coupling kit (A515, Dojindo Molecular Technologies), which activated the carboxy-end of the CA SAM, formed active ester, and induced the binding reaction of the Abs with the ester. The residual activated ester was terminated using a blocking solution in the kit.

In addition to the CA SAM, we used Cys-streptavidin (PRO1005, Click Biosystems, TX, USA) to immobilize Abs or nucleic acids with biotin labels. Subsequently, the Cys-streptavidin is studied in terms of its immobilization profile (Section 3.1.1).

FL molecules of HyLite Flour 555 (HL555) and biotins were labeled on IgG-type Abs using commercial kits (LF14 and LK03, Dojindo Molecular Technologies). HL555, which has a light absorption peak at 550 nm and a FL emission peak at 566 nm, was first labeled on the Abs; succeedingly, biotin was labeled on the HL555-labeled Abs. The double labeling did not affect the performance of the labels. In FL detection experiment, commercially available Alexa Flour 555 (AF555)-labeled, goat-polyclonal, anti-mouse IgG (ab150114, Abcam) was biotinylated using the kit described above. The FL molecules of AF555 has almost the same light absorption and FL emission wavelengths as HL555.

The nucleic acids employed in this study were commercially synthesized oligonucleotides (Eurofins Genetics, Tokyo, Japan) that were purified through high-performance liquid chromatography. A FL label, named HEX, which is optically similar to HL555, was added to the 5′-end of the probe single-strand DNA (ssDNA). The target ssDNA complementary to the probe was biotinylated at the 3′-end. Note that DNAs can be biotinylated using commercially available kits; therefore, the present setting of the target is not a loss of generality. The oligonucleotides were delivered in lyophilized forms, reconstituted at 100 $\mu$M with RNase-free TE buffer, pH 8.0 (AM9849, ThermoFisher Scientific, MA, USA), aliquoted into several small volumes, and preserved at − 20 °C until they were used in the experiment.

### 2.4. Optical measurement

Immobilization profiles of protein molecules on flat gold surfaces were measured using a surface plasmon resonance (SPR) instrument (BIACORE-X100, General Electric Healthcare, IL, USA). The immobilized amount can be estimated quantitatively, based on the temporal profiles of binding proteins and target IgG on a flat gold surface (Section 3.1.1).

FL spectra were measured in an illumination-and-collection setup using a set of a monochromator (IsoPlane 160, Princeton Instruments, NJ, USA) and a charge-coupled device (CCD) camera equipped with a cooling unit (ProEM 1200B, Princeton Instruments). Using FL bandpass filters, the wavelength range of 562–620 nm was selectively observed. FL was excited using continuous-wave laser light at 532 nm; the excitation light and FL were focused and collected, respectively, using an objective lens of numerical aperture of 0.14 (M PLAN APO NIR 5× , Mitsutoyo, Kanagawa, Japan).

FL images were captured using a CCD camera (INFINITY 3S, Lumenera, Ottawa, Canada), which was manufactured for loading onto optical microscopes and was not equipped with any cooling unit. FL bandpass filters were set, similarly to the measurement of the FL spectra. Excitation light came from a light-emitting device, which had an emission peak at 527 nm, and was restricted to a band from 515 to 540 nm using bandpass filters. The configurations of the FL spectra and images are available in a previous report (Iwanaga (2020)).

### 2.5. Numerical techniques

Optical responses such as the reflectance, transmittance, and diffraction efficiency of the SC metasurfaces were numerically calculated by employing the rigorous coupled-wave analysis method (Li (1997)), which was combined with scattering-matrix algorithm (Li (1996)) to stably implement the computation for stacked layer structures. The designs of the SC metasurfaces were based on the numerical simulations. Incident light comes from the air side, which is similar to the excitation light in Fig. 1A. The numerically calculated reflectance spectra are provided in the supplementary data (Appendix A). In addition, the resonant EM-field distributions were evaluated using the same code. The complex permittivities of gold and silicon were taken from literature (Rakić et al. (1998); Palik (1991)). The permittivities of air and silicon dioxide were set to their representative values of 1.00054 and 4.5437, respectively, which do not have the imaginary parts.

## 3. Results and discussion

### 3.1. IgG detection

#### 3.1.1. Immobilization profile

To clarify the basic immobilization properties on gold surface, we conducted SPR measurement. Specifically, we measured immobilization profile of the Cys-streptavidin and doubly-labeled human-polyclonal $IgG_1\kappa$ (ab206202, Abcam, Cambridge, UK) on a flat gold surface using the SPR instrument. The measured temporal profile is shown in Fig. 2A. First, phosphate-buffered saline (PBS), pH 7.4 (164–25511, FUJIFILM Wako Pure Chemical, Osaka, Japan) was flowed to fill the MF path and the Cys-streptavidin diluted to 200 $\mu$g mL$^{-1}$ with the PBS was flowed at a rate of 10 $\mu$L min$^{-1}$ for 10 min. After rinsing the MF path with the PBS, the doubly labeled $IgG_1\kappa$ of 5 $\mu$g mL$^{-1}$ was flowed at 10 $\mu$L min$^{-1}$ for 10 min; the $IgG_1\kappa$ was label with HL555 and biotin, as noted in Section 2.3.

ΔRU in Fig. 2A represents the absorbed protein mass per unit area and is in the units of pg mm$^{-2}$. The ΔRU of Cys-streptavidin and doubly labeled $IgG_1\kappa$ were 5805.8 and 3069.3, respectively. Considering the molecular weights (Cys-streptavidin, 17.9 kDa; $IgG_1\kappa$, 146 kDa), the ΔRU values means that one Cys-streptavidin monomer was located in a square of 2.24 × 2.24 nm$^2$ on average and one $IgG_1\kappa$ molecule in 8.77 × 8.77 nm$^2$. Thus, it was confirmed that the immobilizations occurred efficiently. The rinse with the PBS did not decrease ΔRU, which indicates that unbound molecules hardly existed near the gold surface. The SPR measurement was conducted more than twice and resulted in almost the same data.

#### 3.1.2. Enhanced FL on SC metasurface

Optical resonances in the SC metasurfaces are observed in the reflectance spectra shown in Fig. 2B; solid and broken curves show the reflectance spectra for air-hole diameters of 300 and 260 nm, respectively. The spectra were measured at an incident angle of 5°, which was confirmed to be almost equivalent to the normal incidence in a previous report (Iwanaga and Choi (2015)) and was set as such because of the limitation in the setup of the spectrometer. The reflectance spectra were measured more than twice and were almost identical to each other. Fig. 2C shows enhanced FL spectrum emitted from FL-labeled IgG on a SC metasurface. The FL label was introduced using the HL555 labeling kit.

When measuring the FL spectra in Fig. 2C, we conducted the following MF procedure. Preflow for 15 min with a bovine serum albumin (BSA) blocker (37525, ThermoFisher Scientific), which was diluted 10 times with the PBS and adjusted to 1% BSA. Successively,

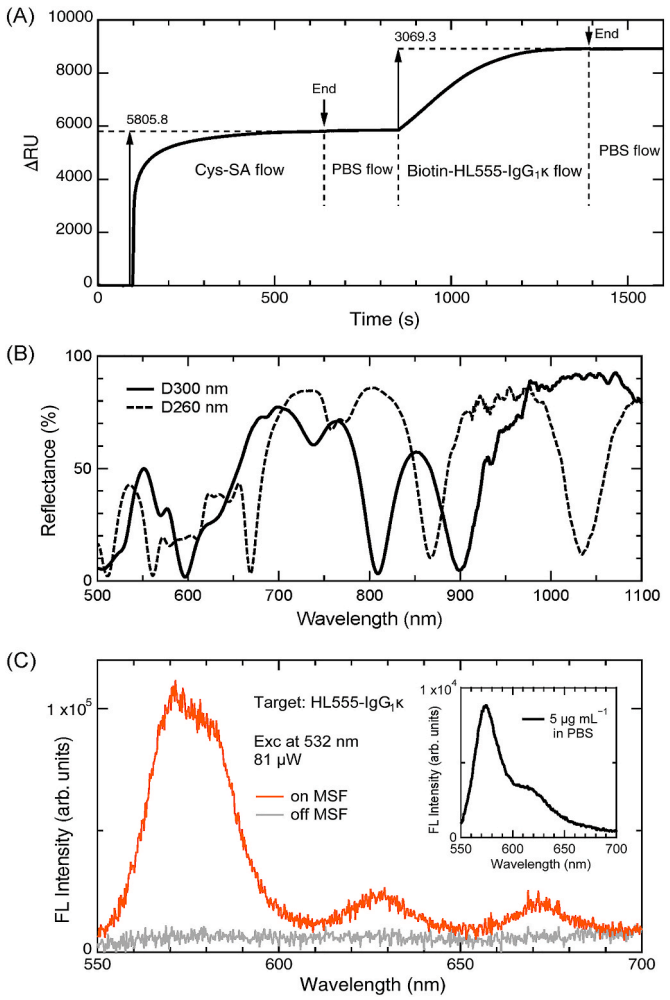


**Fig. 2.** (A) Immobilization profile of Cys-streptavidin (Cys-SA) and double labeled immunoglobulin $G_1\kappa$ ($IgG_1\kappa$) on flat gold surface. Profile was measured using a surface-plasmon-resonance instrument. (B) Measured reflectance spectra of SC metasurfaces with air-hole diameter (D) of 300 and 260 nm, shown with solid and broken curves, respectively. Spectra were measured at the almost normal incidence. (C) Resonantly enhanced FL spectrum measured on SC metasurface, shown with orange line. Target was HyLite-555-labeled $IgG_1\kappa$ (HL555-$IgG_1\kappa$). Spectrum off SC metasurface is also shown with gray curve near bottom, which indicates background level and does not contain any FL component. Inset shows FL spectrum of HL555-$IgG_1\kappa$ at 5 $\mu$g mL$^{-1}$ in phosphate-buffer saline. (For interpretation of the references to color in this figure legend, the reader is referred to the Web version of this article.)

Protein AG-Cys (PRO1001, ClickBiosystems) was diluted to 73 $\mu$g mL$^{-1}$ with the PBS and flowed for 20 min; HL555-$IgG_1\kappa$ of 50 ng mL$^{-1}$ was flowed for 32 min; the MF paths were rinsed with pure water for 20 min; dry $N_2$ gas was flowed for 40 min. The flow rates were approximately 10 $\mu$L min$^{-1}$.

The SC metasurface had air holes of diameter 260 nm. The FL spectra on and off the SC metasurface are shown with orange and gray lines, respectively; the excitation power was 81 $\mu$W on the sample. First, no detectable FL signal was observed when the excitation light was off the metasurface; second, the FL spectrum on the metasurface was substantially modified in shape from the original FL spectra of HL555 in the inset of Fig. 2C. The enhanced shoulder at 580 nm and the peaks at 630 and 680 nm corresponded to the resonances observed in the reflectance spectrum in Fig. 2B, where the resonances contributing to the FL enhancement appeared as small dips or a shoulder. Note that a deep dip at 598 nm originates from the Fabry-Perot-type interference and is not a resonance to enhance FL. The FL spectra on the SC metasurface were measured at least at five different focal points and observed in almost the same spectral shape. The original FL spectrum of HL555 was measured using the HL555-$IgG_1\kappa$ that was unbound in the PBS. The liquid specimen was diluted to a concentration of 5 $\mu$g mL$^{-1}$ with the PBS, poured in a transparent cell, and set in the FL measurement setup, which was the same as that for measuring the FL spectra in Fig. 2C.

### 3.1.3. Direct FL detection

A protocol for detecting target Abs is illustrated in Fig. 3A. First, a CA SAM (green lines) was prepared on the outermost gold surface of the SC metasurface, as described in Section 2.3. Second, anti-biotin Abs were immobilized using the amine-coupling kit, as mentioned in Section 2.3. The anti-biotin Abs at 20 $\mu$g mL$^{-1}$ were flowed for 15 min. Third, biotin-labeled target IgGs were flowed at 8–10 $\mu$L min$^{-1}$ for 30 min, coupled with the anti-biotin Abs, and were selectively immobilized on the SC metasurface.

We set the target as a representative antibody of IgG. To test the detection performance of the SC metasurfaces, Alexa Flour 555 (AF555)-labeled IgG was used as the target, which was goat-polyclonal and anti-mouse (ab150114, Abcam). The AF555-labeled IgG was additionally biotinylated using the biotin-labeling kit. Fig. 3B shows a series of FL images taken on the SC metasurfaces; the target concentrations were 100, 5, and 0.25 pg mL$^{-1}$ from left to right, respectively. The images were taken after rinsing the target IgG with the PBS for 10 min. Triangles in each panel indicate defects coming from the imperfect CA SAM (100 and 5 pg mL$^{-1}$) or a particle dust on the top of the PDMS chip (0.25 pg mL$^{-1}$). We avoided the defect area to evaluate the FL intensities.

In Fig. 3C, the measured FL intensity is plotted with closed circles for

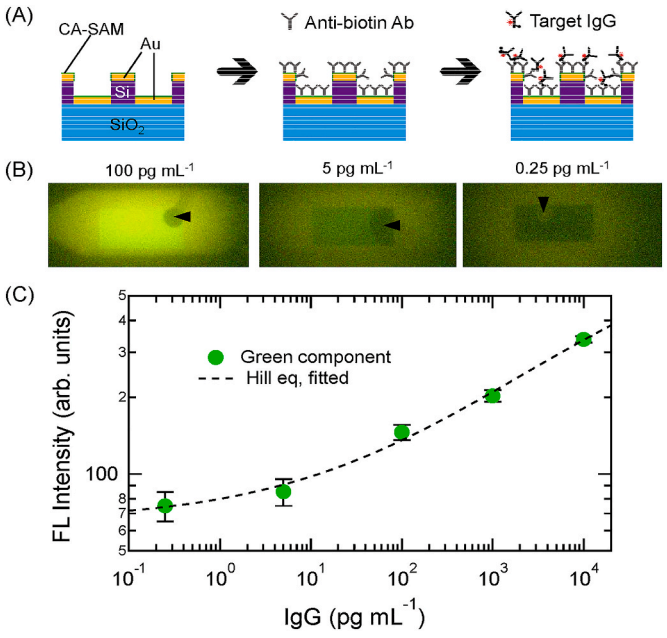


**Fig. 3.** Direct detection of FL-labeled IgG on SC metasurfaces. (A) Schematic illustration of direct IgG detection. After carboxy-acid (CA) self-assembled monolayer (SAM) was grown, binding molecules of anti-biotin antibody (Ab) were immobilized on CA-SAM-coating gold surface. Target IgG, which was doubly labeled with Alexa Flour (AF555) and biotin, was captured by binding molecules and then immobilized on SC metasurface. (B) FL images of different target IgG concentrations of 100, 5, and 0.25 pg mL$^{-1}$. For clarity, brightness was increased by 40% from raw images. Triangles indicate CA-SAM-origin defects on SC metasurface or a particle dust on PDMS chip. (C) Measured FL data (closed circles with error bars) evaluated with avoiding the defects in the FL images (B), plotted for the target IgG concentration in log-log scale, and then fitted with Hill equation (eq. (1)); fitted curve is shown with dashed curve. (For interpretation of the references to color in this figure legend, the reader is referred to the Web version of this article.)

the target IgG concentration in a wide range from 0.25 to 10000 pg mL$^{-1}$, and the error bars are shown. The errors primarily originated from thermal noise on the CCD camera without any cooling unit. The data are shown in the log-log scale. Dashed curve is a fitted curve for the measured intensity, using the Hill equation (eq. (1)), as will be described in the next subsection. The fitted curve is approximately a power function in the range above 10 pg mL$^{-1}$; therefore, the measured data more than 5 pg mL$^{-1}$ are almost scaled in the IgG detection. Thus, the detection dynamic range is more than 5 pg mL$^{-1}$, and the practical LOD is 5 pg mL$^{-1}$. The direct detection was repeated more than twice to confirm the low LOD. The high sensitivity is comparable to that of an all-dielectric metasurface FL sensor (Iwanaga (2020)).

### 3.2. Analysis for the detection data

Analysis of the detected FL signals was conducted using the Hill equation (Hill (1910)), which generally describes mass action reaction under equilibrium such as the flow condition in the present study. Note that eq. (1) is mathematically equivalent to the so-called four-parameter logistic equation (Iwanaga (2020)), which is routinely used to analyze results of immunoassays such as ELISA. Currently, the Hill equation (or the four-parameter logistic equation) is understood as an empirical equation that starts from a simple assumption and is able to reproduce experimental data in flexible ways (Gesztelyi et al. (2012)).

Because the FL-signal intensity emitted from the metasurface sensors is proportional to the number of bound targets, the response from the bound targets is approximated by the Hill equation, which enables us to evaluate reactions between receptors and bound targets. The Hill equation is explicitly written as follows.

$$y = y_0 + (S - y_0)\frac{x^n}{x^n + K_D^n} \tag{1}$$

where $y$ denotes the FL-signal intensity, $y_0$ the background level without any target, $S$ the saturation signal intensity, which was regarded as a proportional constant in fitting, $x$ the concentration of target, $n$ the degree of cooperative reaction, and $K_D$ dissociation constant (Gesztelyi et al. (2012); Neubig et al. (2003)). When the degree $n$ is less than unity, the reaction is anti-cooperative, whereas the reaction is cooperative for $n \geq 1$ (Irrera et al. (2018)).

Analysis of the measured data in Fig. 3C using eq. (1) resulted in a parameter set of $y_0 = 65.2$, $S = 920.8$, $n = 0.356$, and $K_D = 87902$. There are five measured data points in Fig. 3C; accordingly, the data were fitted uniquely using eq. (1) on a commercial graphical application. Note that the unit of $K_D$ is pg mL$^{-1}$. Thus, it becomes explicit that the power in the range exceeding 10 pg mL$^{-1}$ is 0.356, which is substantially smaller than 1 and plays a positive role in detecting a wide range of the target concentration. Also, the value of $n$ implies an anti-cooperative reaction between the target IgG and binding molecules.

### 3.3. Anti-p53 Ab detection

Fig. 4A and B illustrate immobilization configurations for target anti-p53 Abs, which are cancer markers for early-stage colorectal cancer (Kuwabara et al. (2011); Ochiai et al. (2012); Yokomizo et al. (2016); Kumamoto et al. (2017); Liu et al. (2020)); the medical diagnosis criterion is set to a few ng mL$^{-1}$. For the proof-of-concept experiment, we used rabbit-polyclonal anti-p53 Abs (ab17990, Abcam) as the target. The anti-p53 Abs were biotinylated using the same biotin-labeling kit as that used for IgG (Fig. 3). Binding molecules are different in the two configurations: rabbit-polyclonal anti-biotin Ab (ab53494, Abcam) in Fig. 4A and streptavidin (434301, ThermoFisher Scientific) in Fig. 4B. The binding molecules were efficiently immobilized using the amine-coupling kit described above (Section 2.3), which is optimized for immobilizing Abs and proteins on the CA SAM. The experiment in each configuration was conducted at least twice.

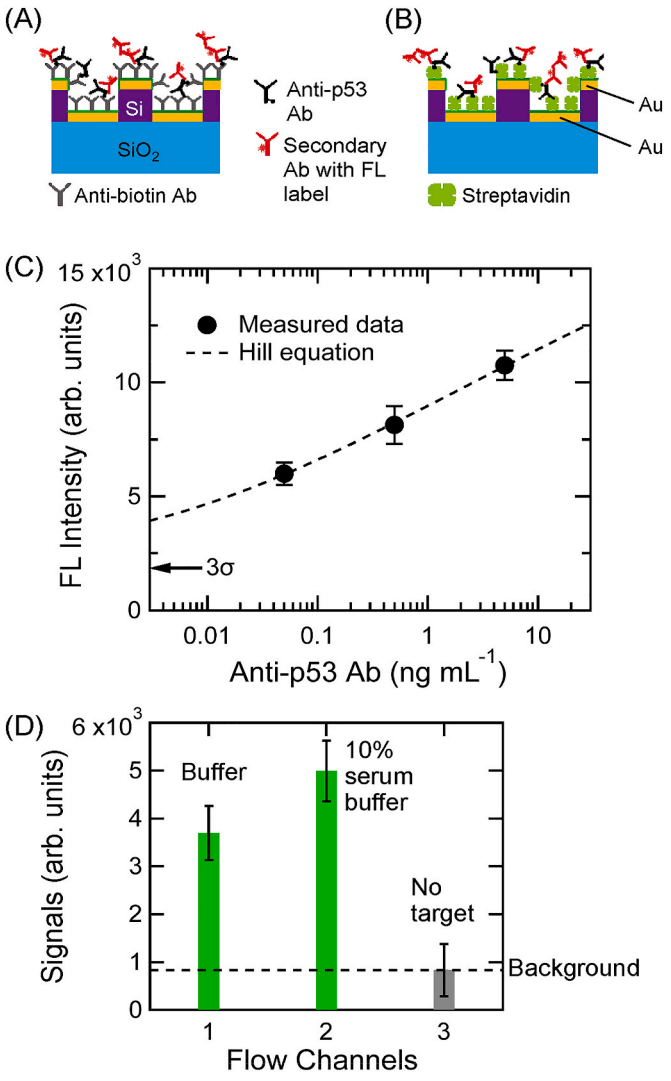


**Fig. 4.** Schematic configurations for indirect detection of anti-p53 Ab using (A) anti-biotin Abs and (B) streptavidin. The target anti-p53 Abs (black) were biotinylated and FL-label-free, and the secondary Abs (red) were labeled with AF555. (C) Indirect detection of FL-label-free anti-p53 Abs, measured in the configuration (A). Measured data (closed circles with error bars) and fitted curve (dashed curve) using Hill equation (eq. (1)) are shown in the semi-log scale. 3$\sigma$ ($\sigma$: standard deviation) from zero FL intensity is indicated by an arrow. (D) Measured FL intensity dependent on solution buffers in configuration (B): NS buffer, 10% human-serum-supplemented NS buffer, and NS buffer without any target anti-p53 Ab, shown at flow channels 1–3, respectively. The target concentration was 5 ng mL$^{-1}$ at channels 1 and 2. Channel 3 is a negative control. Dashed line indicates level of background signal. (For interpretation of the references to color in this figure legend, the reader is referred to the Web version of this article.)

In Fig. 4C, the measured FL intensity is shown with closed circles associated with error bars, and the Hill-equation (eq. (1)) fitting curve is presented with a dashed curve. Note that the data are represented in the semi-log scale. The Hill-fitting curve corresponds to a parameter set of $y_0 = 194.5$, $S = 19596$, $n = 0.224$, and $K_D = 2.37$ ng mL$^{-1}$. The fitting was conducted as follows: first, $y_0$ was determined from the measured data for background; second, the three left parameters were evaluated by fitting the three measured data points in Fig. 4C on the graphical software. In the measured range, the data are almost scaled by a power of 0.224, suggesting that good sensitivity is maintained even at a low target concentration of 50 pg mL$^{-1}$ and that the quantitative analysis is feasible.

In Fig. 4D, buffer dependence of the indirect anti-p53-Ab detection is shown. At flow channel 1, the target was diluted using only NS buffer (ab193972, Abcam), which is a PBS-based buffer of pH 7.4 and is suitable to dilute Abs; at flow channel 2, the target was diluted using 10% human-serum-supplemented NS buffer. The serum used was a pooled batch of serum obtained from 10 individuals (12181201, Cosmo-Bio, Tokyo, Japan). The use of 10% serum-supplemented buffer is practical because it is always possible to prepare it by starting from human serum. At flow channel 3, the target-blank buffer (or pure NS buffer) was flowed. After flowing the target samples and the blank sample, all the channels were rinsed with the PBS for 10 min; afterward, the secondary Abs with FL labels, which were goat-polyclonal anti-rabbit IgG with AF555 labels at 100 ng $mL^{-1}$, were flowed in the three channels at approximately 7 $\mu$L $min^{-1}$ for 15 min; finally, the channels were rinsed with the PBS for 10 min; thereafter, the FL measurement was conducted. As a result, both channels 1 and 2 (green) exhibited definite FL signals in comparison with the channel 3 (gray) without any target. The serum-supplemented buffer did not decrease the FL-signal intensity. Thus, it was confirmed that the SC metasurfaces maintained their function as biosensors even when the buffer included plenty of impeding molecules such as albumin. We mention that the 10% serum-supplemented buffer resulted in the increase in the FL-signal intensity; this is probably because much physical absorption of the albumin and proteins in the serum occurred on the PDMS surfaces inside the MF path (see the section view in Fig. 1F) and the secondary FL-labeled Abs absorbed on the physically absorbed biomolecules in non-specific ways. It is known that this kind of non-specific absorption can be avoided by incorporating pretreatment for the PDMS chips to suppress protein absorption. In this study, the PDMS chip did not undergo any pretreatment to avoid physiabsorption.

In Figs. 3C and 4C, the measured data are mostly scaled in the presented ranges. However, in many papers, the LOD has been routinely determined out of the dynamic range, and the values more than one-order smaller than the edge of the scaled ranges were frequently claimed as the LOD. We stress that the conventionally reported LOD does not have practical meaning and believe that detection capability should be discussed in the scaled (or dynamic) ranges.

### 3.4. Detection of complementary DNA (cDNA) to SARS-CoV-2 RNA

We examined capability of the metasurface biosensors to detect nucleic-acid molecules. As examples, oligonucleotide cDNAs to the RNA of SARS-CoV-2 were detected. The immobilization configuration is illustrated in Fig. 5A. As binding molecules, we chose Cys-streptavidin, which was used in the SPR experiment (Fig. 2A). Note that the Cys-streptavidin can directly bind gold surfaces via His-tag and does not need CA SAM, as illustrated in Fig. 5A.

Table 1 lists the target and probe DNA sequences used in this experiment. The target sequence is a cDNA to a part of the RNA of SARS-CoV-2, which was originally chosen as a primer for reverse-transcript polymerase chain reaction (RT-PCR) (Shirato et al. (2020)). The probe is complementary to the target and has a FL label at the 5′ end. As mentioned earlier (Section 2.3), the target was designed to have a biotin label at the 3' end. The DNAs have 20 bases and their melting temperature $T_m$ of 53 °C, which was evaluated from an approximated equation for $T_m$ (Wetmur (1991)). To hybridize the target and probe DNAs, after initial pulse heating at 80 °C for 5 min, we set the temperatures to ($T_m$ − 5) °C for 30 min and then ($T_m$ − 10) °C for 30 min. The probe was diluted to 500 nM with a mixed buffer, SSC, pH 7.0 (15557044, ThermoFisher Scientific) and the TE buffer, pH 8.0 at a volume ratio 1 : 3. The composition of the SSC buffer was 3.0 M sodium chloride and 0.3 M sodium citrate. The targets were diluted to a range from 0.05 to 5 nM with the mixed buffer of the SSC-TE mixed buffer and aqueous solution containing 1% sodium dodecyl sulfate (SDS) at a volume rato 9 : 1. The SDS solution was originally 10% SDS (24730020, ThermoFisher Scientific).

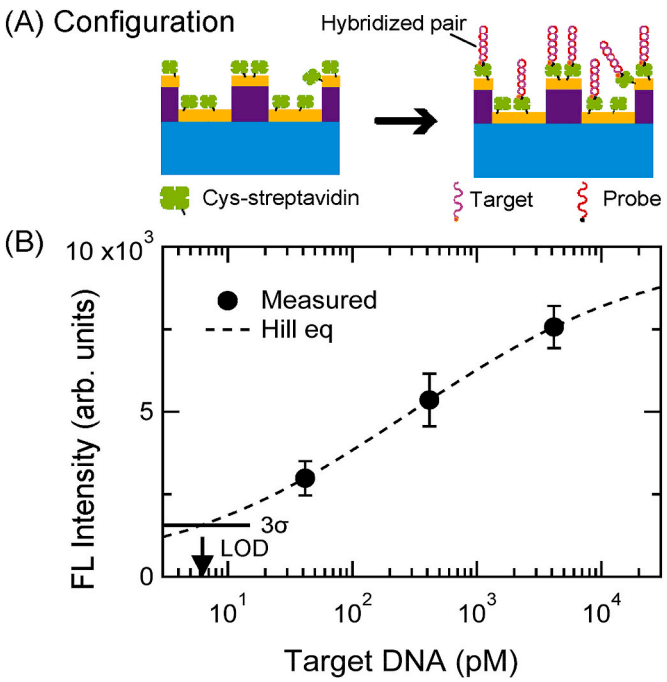


**Fig. 5.** Detection of oligosynthesized complementary DNA (cDNA) to RNA of SARS-CoV-2. (A) Configuration of immobilized DNA pairs, which are hybridized pairs of the target and probe. (B) Detection results. Measured data are shown using closed circles with error bars. Fitted curve using Hill equation (eq. (1)) is shown with dashed curve. Horizontal axis represents net concentration of target cDNA flowed on SC metasurfaces. LOD indicated by arrow was estimated to be 6.3 pM from cross point of Hill curve and 3$\sigma$ level is shown with horizontal bar.

**Table 1**
DNA sequences complementary to SARS-CoV-2 RNA. Target sequence was taken from literature (Shirato et al. (2020)). [BIO] stands for a biotin label added at the 3′ end. [HEX] denotes a FL label, having similar optical properties to HL555, added at the 5′-end.

| Role of DNA | Sequence (5′ to 3′) |
|---|---|
| Target | AAATTTTGGGGACCAGGAAC[BIO] |
| Probe | [HEX]GTTCCTGGTCCCCAAAATTT |

The MF protocol for the cDNA detection was as follows. First, the PBS was flowed for 5 min to fill the MF paths with liquid; the zero level was measured in the FL-imaging setup; the Cys-streptavidin diluted to 20 $\mu$g $mL^{-1}$ with the PBS was flowed at approximately 5 $\mu$L $min^{-1}$ for 40 min; the channels were rinsed with the PBS for 10 min; the liquid solution containing the hybridized pairs of the target and probe were flowed at 3.8–4.5 $\mu$L $min^{-1}$ for 1 h; finally, the channels were rinsed with the SSC-TE mixed buffer for 5 min. The net concentrations of the target were 4160, 416, and 41.6 pM (or fmol $mL^{-1}$) in the channels 1–3, respectively. The FL measurement was carried out immediately after the final rinse. The experiment was conducted more than twice.

In Fig. 5B, the FL-detection data are plotted in the semi-log scale, using closed circles with error bars; each data point was subtracted with the measured background level; the horizontal axis represents the net target concentration flowed in the MF system. The measured data including the zero target data (not shown, because of the logarithmic horizontal axis) were fitted with the Hill equation (eq. (1)), shown with a dashed curve, and were well reproduced. The Hill parameters were $y_0 = 0$, $S = 9950.4$, $n = 0.435$, and $K_D = 292.5$ pM. The fitting of the parameters was implemented in a similar way to that shown in Fig. 4C; the experimentally determined background was first set to 0 (*i.e.*, $y_0 = 0$), and then the three left parameters were evaluated through fitting the

three data points in Fig. 5B. Notably, the presented data are almost scaled in Fig. 5B. A horizontal bar in Fig. 5B indicates the $3\sigma$ ($\sigma$: standard deviation) level determined from the no target data in the measurement. From the cross point of the $3\sigma$ level and the Hill curve, the LOD for the cDNA target is estimated to be 6.3 pM. Although the LOD is a small value in direct detection techniques, it is larger than that in amplification-incorporated techniques such as RT-PCR. A future work will be to connect the metasurface biosensors to an amplification technique. The length of the DNAs is short, which suggests that the SC metasurfaces have potential as a platform for microRNA (miRNA) detection.

Since the LOD in Fig. 5B comes from direct detection, we discuss and compare it those of other direct sensing techniques in terms of the dynamic ranges. Plasmon-based sensing has been extensively reported. Focusing only on nucleic-acid detections, we refer to the three following results. (1) ssDNAs of salmon sperm were immobilized on gold nanodisks covered with $\alpha$-$Si_{0.8}C_{0.2}$ and hybridized with the complementary ssDNA for 4 h (Touahira et al. (2010)); plasmon-enhanced FL images at only 5 nM and 5 fM were shown and the detection at 5 fM was claimed. The dynamic range is unknown from the data. In addition to the long hybridization time, the high sensitivity implies that the layer of $\alpha$-$Si_{0.8}C_{0.2}$ plays a positive role in assisting the hybridization by, for example, attractive electrostatic force. (2) An extremely high sensitivity of 100 aM for miRNA was reported after very long-time incubation, *i.e.*, overnight incubation (Joshi et al. (2015)). They used triangular gold nanoparticles and conducted the sensing with measuring resonant wavelength shifts, similar to SPR measurement. The dynamic range is unclear from the results; for example, the resonant shifts at 100 pM and 10 pM cannot be discriminated, that is, the measured data were not scaled below 100 pM. Thus, it is difficult to calibrate the target concentrations below 100 pM from the measured shifts. (3) A short incubation time of 1 h was reported for miRNA detection on gold nanoparticles and the LOD was claimed to be 1 pM from the measured resonant wavelength shifts (Miti et al. (2020)). The data show that the shifts are out of the dynamic range at 100 pM; in fact, the shifts at 100 pM and 1 pM are not discriminated statistically. Therefore, it is unlikely to specify the detected concentration for the samples at concentrations below 100 pM.

Summing up the three abovementioned reports, we can declare that the target concentrations at 100 pM were detected in the scaled ranges, whereas no explicit report has shown a calibrated detection curve below 100 pM. The present result exhibits the series of scaled data, and furthermore the LOD is estimated to be 6.3 pM (Fig. 5B). Thus, the SC metasurface is one of the most efficient plasmonic platforms to detect nucleic acids in a direct manner and can offer quantitative detection for targets at low concentrations below 100 pM.

In addition to the plasmonic platforms, an efficient DNA sensor made of an all-dielectric metasurface was recently reported, and the LOD in the direct detection was estimated to be 0.11 pM (Iwanaga (2021)). The better performance probably comes in part from the protuberant structure, in comparison with the hole-array structure in the SC metasurfaces.

## 4. Conclusions

We have experimentally tested the SC metasurfaces as practical biosensors for a wide range of targets from Abs to DNAs. It was shown that the detection capability is quite high for a typical Ab of IgG, which was detected in a scaled manner even at 5 pg $mL^{-1}$, and that the cancer marker anti-p53 Ab was detected even at 50 pg $mL^{-1}$, which is far lower than the medical criterion of a few ng $mL^{-1}$. It was moreover shown that cDNAs to the RNA of SARS-CoV-2 were detected on the range of fmol $mL^{-1}$ in a scaled manner; the LOD was estimated to be 6.3 fmol $mL^{-1}$ from the analysis. Overall, the SC metasurfaces work as sufficiently efficient biosensors for the practical Ab markers and can also directly detect nucleic acids in a short immobilization time of 1 h in a scaled manner. Although we have presented proof-of-concept experiments that were designed to conduct direct or indirect detection of the targets and were rather simple, more practical assays such as sandwich configurations are feasible on the SC metasurfaces as straightforward extensions of this study.

## Declaration of competing interest

The author declares that he has no competing financial interests or personal relationships that could influence the contents in this paper.

## Acknowledgments

We would like to thank Naga Anirudh Peyyety for the contribution to this study at the initial stage, Naoki Ikeda and Jun Matsuzawa for technical support in the nanofabrication of metasurfaces, and Saki Ishihara and Hiroshi Takenaka for technical assistance in the biosensing on metasurfaces. This study was partially supported by JSPS KAKENHI Grant number JP17H01066, by HPCI system research project (IDs: hp170134, hp180107, hp190037) enabling us to use supercomputers at Cyberscience Center, Tohoku University, and by the fourth mid-term and M-CUBE projects in NIMS. Nanofabrication processes were conducted in part at Namiki Foundry and Nanofabrication Platform in NIMS.

## Appendix A. Supplementary data

Supplementary data to this article can be found online at https://doi.org/10.1016/j.bios.2021.113423.

## References

Bauch, M., Toma, K., Toma, M., Zhang, Q., Dostalek, J., 2014. Plasmon-enhanced fluorescence biosensors: a review. Plasmonics 9, 781–799.
Choi, B., Iwanaga, M., Miyazaki, H.T., Sugimoto, Y., Ohtake, A., Sakoda, K., 2015. Overcoming metal-induced fluorescence quenching on plasmo-photonic metasurfaces coated by a self-assembled monolayer. Chem. Commun. 51, 11470–11473.
Fu, C.C., Ossato, G., Long, M., Digman, M.A., Gopinathan, A., Lee, L.P., Gratton, E., Khine, M., 2010. Bimetallic nanopetals for thousand-fold fluorescence enhancements. Appl. Phys. Lett. 97, 203101.
Gesztelyi, R., Zsuga, J., Kemeny-Beke, A., Varga, B., Juhasz, B., Tosaki, A., 2012. The Hill equation and the origin of quantitative pharmacology. Arch. Hist. Exact Sci. 66, 427–438.
Giljohann, D.A., Mirkin, C.A., 2009. Drivers of biodiagnostic development. Nature 462, 461–464.
Greffet, J.J., Nieto-Vesperinas, M., 1998. Field theory for generalized bidirectional reflectivity: derivation of helmholtz's reciprocity principle and Kirchhoff's law. J. Opt. Soc. Am. A 15, 2735–2744.
Hill, A.V., 1910. The possible effects of the aggregation of the molecules of haemoglobin on its dissociation curves. J. Physiol. (Lond.) 40 (Proceedings iv–vii).
Irrera, A., Leonardi, A.A., Di Franco, C., Lo Faro, M.J., Palazzo, G., D'Andrea, C., Manoli, K., Franzò, G., Musumeci, P., Fazio, B., Torsi, L., Priolo, F., 2018. New generation of ultrasensitive label-free optical Si nanowire-based biosensors. ACS Photonics 5, 471–479.
Iwanaga, M., 2016. Plasmonic Resonators: Fundamentals, Advances, and Applications. Pan Stanford Publishing, Singapore.
Iwanaga, M., 2020. All-dielectric metasurface fluorescence biosensors for high-sensitivity antibody/antigen detection. ACS Nano 14, 17458–17467.
Iwanaga, M., 2021. High-sensitivity high-throughput detection of nucleic-acid targets on metasurface fluorescence biosensors. Biosensors 11, 33.
Iwanaga, M., Choi, B., 2015. Heteroplasmon hybridization in stacked complementary plasmo-photonic crystals. Nano Lett. 15, 1904–1910.
Iwanaga, M., Choi, B., Miyazaki, H.T., Sugimoto, Y., 2016. The artificial control of enhanced optical processes in fluorescent molecules on high-emittance metasurfaces. Nanoscale 8, 11099–11107.
Iwanaga, M., Choi, B., Miyazaki, H.T., Sugimoto, Y., Sakoda, K., 2015. Large-area resonance-tuned metasurfaces for on-demand enhanced spectroscopy. J. Nanomater. 2015, 507656.
Joshi, G.K., Deitz-McElyea, S., Liyanage, T., Lawrence, K., Mali, S., Sardar, R., Korc, M., 2015. Label-free nanoplasmonic-based short noncoding RNA sensing at attomolar concentrations allows for quantitative and highly specific assay of microrna-10b in biological fluids and circulating exosomes. ACS Nano 9, 11075–11089.
Kinkhabwala, A., Yu, Z., Fan, S., Avlasevich, Y., Müllen, K., Moerner, W.E., 2009. Large single-molecule fluorescence enhancements produced by a bowtie nanoantenna. Nat. Photonics 3, 654–657.

Kneipp, K., Wang, Y., Kneipp, H., Perelman, L.T., Itzkan, I., Dasari, R.R., Feld, M.S., 1997. Single molecule detection using surface-enhanced Raman scattering (SERS). Phys. Rev. Lett. 78, 1667–1670.
Kumamoto, K., Ishida, H., Kuwabara, K., Amano, K., Chika, N., Okada, N., Ohsawa, T., Kumagai, Y., Ishibashi, K., 2017. Clinical significance of serum anti-p53 antibody expression following curative surgery for colorectal cancer. Mol. Clin. Oncol. 7, 595–600.
Kuwabara, K., Kumamoto, K., Ishibashi, K., Ohsawa, T., Kumagai, Y., Baba, H., Tsuji, Y., Haga, N., Ishida, H., 2011. Clinical significance of serum anti-p53 antibody measurement for colorectal cancer. Gan To Kagaku Ryoho 39, 2167–2169 (in Japanese).
Kyo, M., Usui-Aoki, K., Koga, H., 2005. Label-free detection of proteins in crude cell lysate with antibody arrays by a surface plasmon resonance imaging technique. Anal. Chem. 77, 7115–7121.
Lakowicz, J.R., Ray, K., Chowdhury, M., Szmacinski, H., Fu, Y., Zhang, J., Nowaczyk, K., 2008. Plasmon-controlled fluorescence: a new paradigm in fluorescence spectroscopy. Analyst 133, 1308–1348.
Li, L., 1996. Formulation and comparison of two recursive matrix algorithm for modeling layered diffraction gratings. J. Opt. Soc. Am. A 13, 1024–1035.
Li, L., 1997. New formulation of the Fourier modal method for crossed surface-relief gratings. J. Opt. Soc. Am. A 14, 2758–2767.
Liu, S., Tan, Q., Song, Y., Shi, Y., Han, X., 2020. Anti-p53 autoantibody in blood as a diagnostic biomarker for colorectal cancer: a meta-analysis. Scand. J. Immunol. 91, e12829.
Miti, A., Thamm, S., Muller, P., Csaki, A., Fritzsche, W., Zuccheri, G., 2020. A miRNA biosensor based on localized surface plasmon resonance enhanced by surface-bound hybridization chain reaction. Biosens. Bioelectron. 167, 112465.
Neubig, R.R., Spedding, M., Kenakin, T., Christopoulos, A., 2003. International union of pharmacology committee on receptor nomenclature and drug classification. XXXVIII. Update on terms and symbols in quantitative pharmacology. Pharmacol. Rev. 55, 597–606.
Nie, S., Emory, S.R., 1997. Probing single molecules and single nanoparticles by surface-enhanced Raman scattering. Science 275, 1102–1106.
Ochiai, H., Ohishi, T., Osumi, K., Tokuyama, J., Urakami, H., Seki, S., Shimada, A., Matsui, A., Isobe, Y., Murata, Y., Endo, T., Ishii, Y., Hasegawa, H., Matsumoto, S., Kitagawa, Y., 2012. Reevaluation of serum p53 antibody as a tumor marker in colorectal cancer patients. Surg. Today 42, 164–168.
Palik, E.D., 1991. Handbook of Optical Constants of Solids II. Academic, San Diego, USA.
Punj, D., Mivelle, M., Moparthi, S.B., van Zanten, T.S., Rigneault, H., van Hulst, N.F., García-Parajó, M.F., Wenger, J., 2013. A plasmonic 'antenna-in-box' platform for enhanced single-molecule analysis at micromolar concentrations. Nat. Nanotechnol. 8, 512–516.
Rakić, A.D., Djurušić, A.B., Elazar, J.M., Majewski, M.L., 1998. Optical properties of metallic films for vertical-cavity optoelectronic devices. Appl. Opt. 37, 5271–5283.
Schmelzeisen, M., Zhao, Y., Klapper, M., Müllen, K., Kreiter, M., 2010. Fluorescence enhancement from individual plasmonic gap resonances. ACS Nano 4, 3309–3317.
Shirato, K., Nao, N., Katano, H., Takayama, I., Saito, S., Kato, F., Katoh, H., Sakata, M., Nakatsu, Y., Mori, Y., Kageyama, T., Matsuyama, S., Takeda, M., 2020. Development of genetic diagnostic methods for detection for novel coronavirus 2019 (ncov-2019) in Japan. Jpn. J. Infect. Dis. 73, 304–307.
Touahira, L., Galopinb, E., Boukherroubb, R., Gouget-Laemmela, A.C., Chazalviela, J.N., Ozanama, F., Szunerits, S., 2010. Localized surface plasmon-enhanced fluorescence spectroscopy for highly-sensitive real-time detection of dna hybridization. Biosens. Bioelectron. 25, 2579–2585.
Wetmur, J.G., 1991. DNA probes: applications of the principles of nucleic acid hybridization. Crit. Rev. Biochem. Mol. Biol. 26, 227–259.
Yokomizo, H., Yoshimatsu, K., Yano, Y., Okayama, S., Sakuma, A., Satake, M., Yamada, Y., Matsumoto, A., Fujimoto, T., Usui, T., Yamaguchi, K., Shiozawa, S., Shimakawa, T., Katsube, T., Kato, H., Naritaka, Y., 2016. Clinical significance of serum p53 antibody measurement in colorectal cancer patients. Gan To Kagaku Ryoho 43, 1301–1303 (in Japanese).
Zhang, W., Ding, F., Li, W.D., Wang, Y., Hu, J., Chou, S.Y., 2012. Giant and uniform fluorescence enhancement over large areas using plasmonic nanodots in 3D resonant cavity nanoantenna by nanoimprinting. Nanotechnology 23, 225301.
Zhou, L., Ding, F., Chen, H., Ding, W., Zhang, W., Chou, S.Y., 2012. Enhancement of immunoassay's fluorescence and detection sensitivity using three-dimensional plasmonic nano-antenna-dots array. Anal. Chem. 84, 4489–4495.